Epitaxially grown III-arsenide-antimonide nanowires for optoelectronic applications

Dingding Ren[1], Lyubomir Ahtapodov[1], Antonius T. J. van Helvoort[2], Helge Weman[1] and Bjørn-Ove Fimland[1]

[1] Department of Electronic Systems and [2] Department of Physics, Norwegian University of Science and Technology (NTNU), NO-7491 Trondheim, Norway

E-mail: dingding.ren@ntnu.no

Received xxxxxx
Accepted for publication xxxxxx
Published xxxxxx

Abstract

Epitaxially grown ternary III-arsenide-antimonide (III-As-Sb) nanowires (NWs) are increasingly attracting attention due to their feasibility as a platform for the integration of largely lattice-mismatched antimonide-based heterostructures while preserving the high crystal quality. This and the inherent bandgap tuning flexibility of III-As-Sb in the near- and mid-infrared wavelength regions are important and auspicious premises for a variety of optoelectronic applications. In this review, we summarize the current understanding of the nucleation, morphology-change and crystal phase evolution of GaAsSb and InAsSb NWs and their characterization, especially in relation to Sb incorporation during growth. By linking these findings to the optical properties in such ternary NWs and their heterostructures, a brief account of the ongoing development of III-As-Sb NW-based photodetectors and light emitters is also given.

Keywords: GaAsSb, InAsSb, nanowire, optoelectronics

1. Introduction

Nanowires (NWs), characterized by nanoscale diameter, high aspect ratio and large surface-to-volume ratio, are considered premier building blocks for a variety of future nanoelectronic and nanophotonic devices with potential application areas ranging from biomedicine to quantum information technology. Due to the unique 1D or quasi 1D geometry with nanoscale footprint, NWs can circumvent the stringent lattice matching criteria for thin film epitaxial growth, bringing about a powerful vehicle for monolithical integration of highly lattice-mismatched materials with high crystal quality. The direct bandgap of most III-V materials and the ability to exercise precise control of the NW morphology and position on the growth substrate are further critical advantages that facilitate the successful realization of NW-based optoelectronic devices. III-As and III-Sb in particular are among the most promising semiconductors for NW-based applications. Utilizing these binary material systems, the most efficient NW-based solar cell by direct bottom-up growth method reported to date is made from GaAs [1], and the fascinating concept of the Majorana fermion has been explored using InSb NWs [2]. Going beyond binary III-V materials, greater flexibility and tunability of the NW properties can be achieved by alloying additional elements. Ternary and quaternary III-V systems provide an extended platform that is a natural choice for the exploration of new possibilities for III-V NW applications.

III-As-Sb NWs, especially the ternary alloys InAsSb and GaAsSb, have been the focus of extensive research lately. It has been shown that InAsSb can have much higher electron mobility than InAs [3], and the strongest spin-orbit interaction has been experimentally achieved at intermediate Sb contents in zinc blende (ZB) InAsSb NWs, exceeding that of both InAs

and InSb binary materials. In addition, GaAsSb-based NW superlattices have shown single-mode lasing at room temperature with record-low threshold for III-V NWs [4], rendering III-As-Sb NWs of great promise for future light sources and photodetectors.

Ten years has passed since the first explorations in the III-As-Sb NW growth and quite a few prototype devices have been reported. Thus, a dedicated and comprehensive review is needed that specifically summarizes on the growth and optoelectronic applications of III-As-Sb NWs, especially the GaAsSb- and InAsSb-based NWs. In this review, we will go further than previous reviews on III-Sb NWs [5,6], which mainly described the growth of binary NWs and their physical characteristics. Here, we will elaborate on the effects induced by the incorporation of the third element, Sb, and the change of properties for III-As-Sb ternary NW growth. By further reviewing the band structures and optical transitions/properties, we will discuss the current development of photodetectors and light emitters based on GaAsSb and InAsSb NWs in the end.

2. The growth of III-As-Sb NWs

An essential step in the successful realization of III-As-Sb NW devices is to grow the structure in a controlled manner. Most early results focused on the introduction of Sb based on the growth conditions of binary III-As NWs.[7–10] This utilized the fast development of GaAs and InAs NW growth using metalorganic vapor-phase epitaxy (MOVPE) and molecular beam epitaxy (MBE) on both III-V and Si substrates.[11–15]

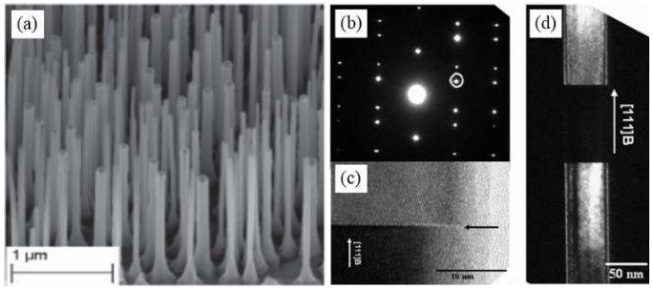

Figure 1. (a) 45° tilted-view SEM image of as-grown GaAsSb NWs grown on GaAs(111)B by Au-catalyzed MBE. (b) Electron diffraction pattern showing the ZB structure with twins. (c) High-resolution TEM image of the ZB crystal phase with a twin plane formed in the center. (d) Dark-field image obtained by using the (1-11) diffraction spot, marked by a circle in (b), where the contrast come from different twins. (Adapted with permission from [7]. Copyright 2008 IOP publishing.)

The first successful growth of GaAsSb NWs, shown in figure 1(a), was reported by Dheeraj et al. using MBE and a Au-catalyzed growth method.[7,8] The electron diffraction, high-resolution and dark-field transmission electron microscopy (TEM) images in figure 1(b), (c) and (d), respectively, show that the GaAsSb NWs exhibit pure ZB crystal phase, which is surprisingly different from its GaAs counterpart, which exhibits pure wurtzite (WZ) phase. The growth of heterostructures was also achieved in the self-catalyzed growth method by MBE, which presents a trend of ZB to WZ to ZB crystal phase transition in the GaAsSb/GaAs/GaAsSb system.[10]

At the pioneering stage, InAsSb NWs were successfully grown on top of InAs NW stems by MOVPE, covering almost the entire compositional range from InAs to InSb, as exemplified in figure 2.[9] Since the Sb can significantly reduce the contact angle of the catalyst due to the surfactant effect, growth of InAsSb NWs is better promoted with larger contact angle of the catalyst on top of an InAs stem on both InP(111)B and InAs(111)B substrates compared to direct growth without a stem.[6,9,16–18] Similar to the GaAsSb inserts in GaAs NWs, the InAsSb segments also show a tendency to form the ZB crystal phase and the WZ InAs to ZB InAsSb transition has been consistently observed.[16,17]

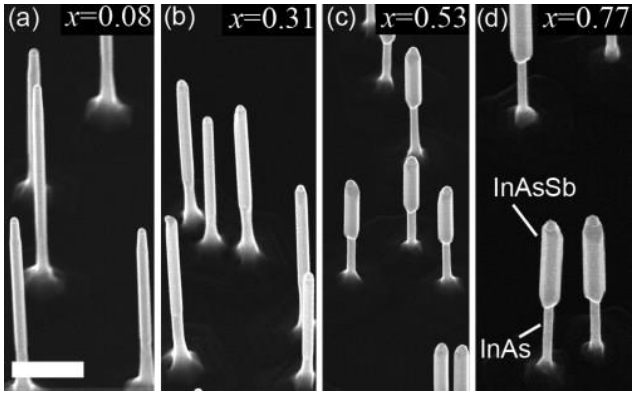

Figure 2. SEM images taken at 30° tilt angle of InAs/$InAs_{1-x}Sb_x$ NWs grown by MOVPE with increasing Sb molar fraction, x=0.08, 0.31, 0.53, and 0.77. The scale bar corresponds to 500 nm. (Reprinted with permission from [9]. Copyright 2011 American Institute of Physics.)

Recently, the direct epitaxial growth of III-As-Sb NWs has been explored on III-V, Si and 2D materials without the use of binary stems. This facilitates further development into integrated NW-based optoelectronic devices. Conesa-Boj et al. used the self-catalyzed method to grow high-yield GaAsSb NW arrays on Si(111) substrate by MBE.[19] Remarkably, the crystal phase is pure ZB down to the first bi-layer on top of Si. Similar to for GaAsSb, a dominant ZB phase has also been observed for InAsSb NWs. Du et al. [20] and Anyebe et al. [21] have grown InAsSb NWs on Si with self-seeded growth methods by MOVPE and MBE, respectively. Both groups reported that the lateral growth of NWs was significantly enhanced with higher Sb flux, and the NW growth could be ended with a film-like morphology when exceeding a specific

flux. Du et al. further explored the MOVPE growth window for InAsSb, and found that the vapor-solid growth mechanism exists under high V/III ratio with low Sb flow rate fraction and the vapor-liquid-solid growth happens under low V/III ratio with high Sb flow rate fraction.[22] By optimizing the growth condition using MBE and MOVPE, Potts et al. [23], Farell et al. [24], Ren et al. [25], and Yang et al. [26] have shown that InAsSb NWs can be grown in a catalyst-free regime that achieves high density on GaAs(111)B, InAs(111)B, InP(111)B and Si(111) substrates for random and positioned array growth. In the window for self-seeded growth, Du et al. explored the planar growth of InAsSb NWs on a Si substrate and showed that the NWs grow along the surface projections of the <111> family of crystal directions and that there exists a strong correlation to the substrate orientation.[27] Besides growth on semiconductor substrates, these NWs can even be grown on graphitic and metal-induced crystalline Si substrates. InAsSb NWs on a graphite substrate show a morphology of aspect ratio over 100 with the assistance of In droplets during nucleation [28], and the growth of GaAsSb NWs on a metal-induced crystalline Si substrate shows a higher density of vertical NWs compared to the GaAs ones [29].

2.1 Sb-induced effects on morphology

A general trend observed with Sb incorporation in III-As-Sb NWs is that a higher Sb content will lead to an enhancement of the radial growth. Using MOVPE, Borg et al. grew a series of Au-catalyzed InAsSb NWs on top of InAs stems and found that the thickness of the InAsSb segment increases with higher Sb molar fraction, as shown in figure 2.[9] They attributed this behaviour to an increased In content in the Au particle that enlarges the NW diameter. Meanwhile, Xu et al. observed a conformal shell formed with higher Sb content over the axial growth of the InAsSb core by the Au-catalyzed method using MBE, leading to a self-formed core-shell NW with complex facets, as shown in figure 3(a).[16] The scanning tunnelling microscopy (STM) images in figure 3(b) and (c) show that there is a surface morphology change from InAs to InAsSb, as marked from region II to III in figure 3(a). This correlates well with the transition of the NW core from WZ InAs to ZB InAsSb with rotational twins, which is illustrated in figure 3(d). The high-resolution STM images in figure 3(e) to (g) clearly show that there is Sb incorporation radially for both the WZ nominal InAs and the ZB InAsSb segments after supplying an Sb flux, and the Sb content is higher in the ZB InAsSb than in the WZ nominal InAs segment. This increased NW thickness with Sb incorporation has also been observed in NWs grown by the self-catalyzed method, indicating that the presence of Sb facilitates the radial NW growth.[19,21,23,30] Density functional theory (DFT) calculations have been performed to reveal the intrinsic mechanisms of increased thickness in GaAsSb NWs, and results show that the Ga binding energy to the side facet of NWs is increased in the presence of Sb adsorbed on NW side facets.[31] This will increase the chance for the Ga adatoms to react with group-V elements and crystalize as radial growth.

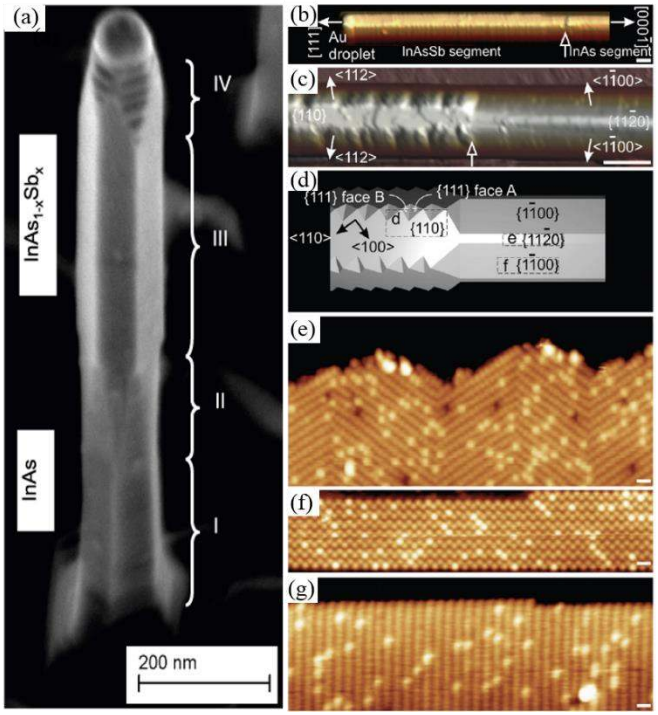

Figure 3. (a) Tilted-view SEM image of an InAs/InAs$_{1-x}$Sb$_x$ NW heterostructure. Complex facets change along the NW axis and are marked with I and II of WZ nominal InAs and III and IV of ZB InAsSb. (b) and (c) are large-scale and close-up three-dimensional (3D) STM images of the NWs containing nominal InAs and InAsSb segments. (d) 3D model close to the interface between the top InAsSb and bottom nominal InAs segments, where the high-resolution STM images (e), (f) and (g) are taken on the NW sidewall of {110}, {11-20} and {1-100} orientations, respectively. The scale bars are 80 nm in (b) and (c) and 1 nm in (e) to (g), respectively. (Adapted with permission from [16]. Copyright 2012 IOP publishing.)

Besides the observation of an increased NW thickness with Sb flux during growth, a reduction in the axial growth rate has also been observed. For MBE growth of self-catalyzed InAsSb NWs on a Si substrate, it has been reported that an increase in Sb flux causes shorter NWs.[21] Further, benefiting from the self-catalyzed growth method for GaAsSb NWs, shown in figure 4, the indirect kinetic influence via the Ga adatom diffusion induced catalyst geometry evolution and the direct composition modulation with Sb incorporation have been proposed to explain the reduced axial growth rate with increased Sb flux.[31] Larger amount of diffused Ga adatoms on the NW sidewalls were consumed as radial growth under higher Sb flux than in GaAs binary NW growth, and fewer Ga adatoms could reach the catalyst particle. This reduces the

contact angle of the Ga droplet and indirectly hampers the As collection efficiency, which slows down the axial growth rate. In addition, the incorporation of Sb will lead to a reduction in the supersaturation for nucleation, which reduces the axial growth rate as well.[31] Notably, the reduction of the supersaturation with Sb incorporation has been further corroborated by Li et al. [31] by varying both As and Sb fluxes for self-catalyzed GaAsSb NWs and by Potts et al. [22] by varying the Sb flux in the growth of catalyst-free InAsSb NWs.

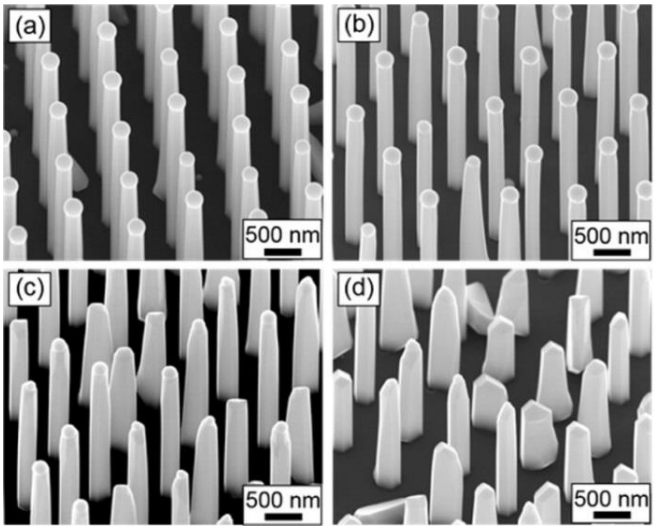

Figure 4. 45° tilted-view SEM images of MBE grown GaAsSb NW arrays grown at 625 °C with Sb_2 flux of (a) 2×10^{-7} Torr, (b) 4×10^{-7} Torr, (c) 6×10^{-7} Torr, and (d) 8×10^{-7} Torr. (Adapted with permission from [31]. Copyright 2016 American Chemical Society.)

Not only during the axial growth but as early as in the nucleation stage can Sb incorporation play an important role for the NW morphology. An Sb-induced reduction of the catalyst contact angle has been proposed by Anyebe et al. that correlates well with the thin film-like growth, instead of NW formation, once the Sb content reaches 14.5 % using MBE.[21] For MOVPE growth, Yuan et al. flushed the surface of GaAs(111)A substrate with trimethylantimony (TMSb) precursor at 420 °C, which helps to adjust the contact angle of the Au catalysts and promote the vertical growth of GaAsSb NWs in (111)A direction, instead of forming crawling surface NWs or tilted NWs in the (111)B direction.[32] Hence, Sb has a pronounced role on the nucleation, the morphology and the catalytic growth of III-As-Sb NWs.

2.2 Sb influence on the crystal phase

One of the most promising features of the NW geometry for applications is the flexibility to tune the crystal phase, which brings about new degrees of freedom to create heterostructures.[33] Different from the binary NWs, whose crystal phase has been suggested and confirmed to be determined by the contact angle of the catalyst [34–36], the incorporation of Sb can lead to a WZ to ZB phase transition, as shown in figure 5(a) and (b) for Au-catalyzed [8] and self-catalyzed growth [10], respectively. Since the incorporation of Sb should lead to a reduction in both the surface energy and the contact angle of the catalyst, resulting in a phase transition in the opposite direction, i.e. ZB to WZ,[31,32,37] the commonly observed WZ to ZB phase transition by adding Sb into binaries should originate from the change in supersaturation.[7,8] With the advent of the self-catalyzed growth method, the crystal phase complexity for quaternary alloys (Au-Ga-As-Sb) in the catalyst can be simplified into ternary systems (Ga-As-Sb), which could further help to figure out the Sb-induced crystal phase effects.[10,31] As documented in the literature, the Ga-As-Sb liquidus isotherm is quite insensitive to the compositional change in Sb compared to As near the self-catalyzed growth condition.[38] Considering an increased chemical potential of the solid phase with Sb incorporation into GaAs, DFT calculations have shown that the supersaturation will be reduced with Sb incorporation, which is in accordance with the composition-dependent pseudobinary liquidus and solidus lines for GaAs-GaSb under equilibrium conditions.[31,39] Besides Sb incorporation, the supersaturation could be further reduced by the enhanced radial growth in the presence of Sb. This results from the radial growth induced contact angle reduction of the catalyst droplet, which causes a reduction in the As collection efficiency and is discussed in Section 2.1. Since a low supersaturation favors ZB formation, this indirect kinetic influence via the Ga adatom diffusion induced catalyst geometry evolution can also facilitate the ZB formation with Sb incorporation. By further applying these effects into the crystal phase diagram between WZ and ZB shown in figure 5(c), the arrow indicates the crystal phase evolution with Sb incorporation into for example GaAs.[31] To further exclude the influence of the contact angle, Sb has been incorporated into very short WZ GaAs stems. This can exclude the Ga diffusion influence due to a very short catalyst to substrate distance, and it indeed shows a WZ to ZB crystal phase transition with a relatively sharp interface from GaAs to GaAsSb, as shown in figure 5(d). We note that the thermodynamic influence on the growth of NWs with ternary or even quaternary material systems can be further studied using computational methods, e.g. the CALPHAD method in combination with DFT calculations.[40,41] Meanwhile, the influence of surface energy can also be exploited using DFT calculations with detailed information on the surface reconstruction, which could be attained by in-situ STM characterization.[42]

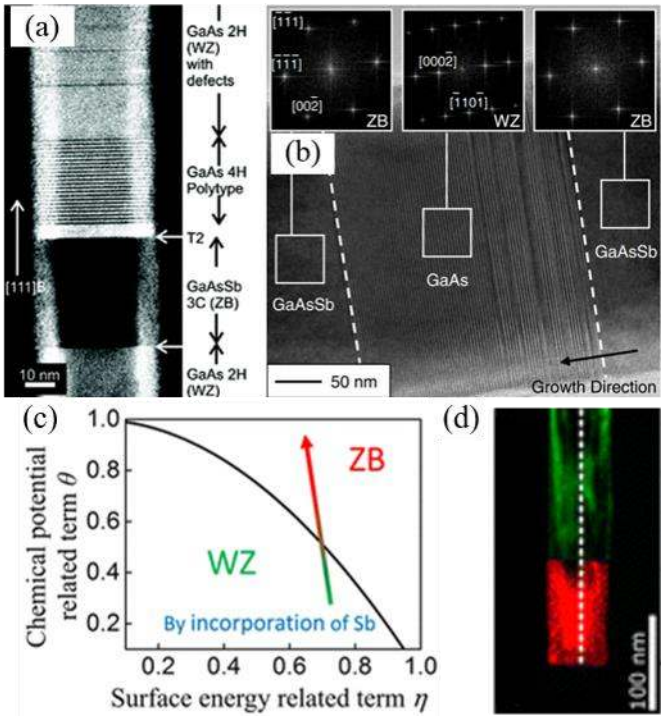

Figure 5. (a) Dark-field STEM of a GaAs/GaAsSb/GaAs heterostructure NW. (Adapted with permission from [8]. Copyright 2008 American Chemical Society.) (b) HRTEM image of the axial GaAsSb/GaAs/GaAsSb heterostructure taken in the <-110> zone axis. Inset FFTs are given for each material, indicating the cubic ZB structure of the GaAsSb and hexagonal WZ structure of the GaAs in the center. Stacking faults are visible at the GaAsSb-GaAs interface but the switch back to GaAsSb is abrupt. (Adapted with permission from [10]. Copyright 2010 American Institute of Physics.) (c) Crystal phase equilibrium diagram, indicating a transition from WZ to ZB by Sb incorporation in GaAs NWs. (d) False-color dark-field image showing a sharp transition from the bottom WZ GaAs, with length around 100 nm, in red, to the top ZB GaAsSb in green. (Adapted with permission from [31]. Copyright 2016 American Chemical Society.).

A dominant WZ to ZB transition due to the supersaturation/compositional influence was discussed in the last paragraph. However, the addition of Sb during growth can also change the contact angle of the catalyst and the surface energy at the growth frontier. This can induce a reverse crystal phase transition, i.e. from ZB to WZ.[43] Hence, fine-tuning the Sb flux, to affect supersaturation, surface energy and contact angle of the catalyst, can be an efficient way to engineer the crystal phase for both WZ and ZB growth in NWs. It has been well accepted that the growth of GaAsSb or InAsSb is one of the most effective methods to acquire stable ZB crystal structure.[8,19,23,26,31,44,45] However, WZ NW growth can be desirable, e.g. in engineering the polarization of light emitted from the GaAs/GaAsSb heterostructured NWs [46]. Due to the difficult controllability of the catalyst, it was for a long time a challenge to grow stable WZ GaAs NWs by the self-catalyzed method. By growing a ZB GaAsSb segment, the contact angle of the catalyst can be reduced such that the growth of WZ GaAs is promoted.[47] This provides an effective way to achieve WZ GaAs NWs without introducing foreign catalysts. Except for the above-mentioned influential factors, the change of surface energy by Sb incorporation could also correlate with the crystal phase evolution. By increasing the Sb flux for self-seeded InAsSb NW growth, the NWs shift preference from ZB to WZ to ZB prevailing crystal phase during the growth.[45] The first ZB to WZ transition can be well explained by the change of the surface energy from ZB to WZ, which can be drawn as a horizontal arrow from right to the left in figure 5(c). In addition, the polarity of the substrate can play an important role in the crystal phase purity of GaAsSb NW growth due to surface energy variations. This can change the contact angle of the catalyst and further influence the possibility of stacking fault formation. By growing GaAsSb NWs on an A-polar GaAs(111) substrate and further controlling the dynamic movement of the Au catalyst to incline on the NW sidewall, kinked Au-catalyzed GaAsSb NWs with ultra-pure ZB crystal phase can be grown.[18,32,43] Notably, also epitaxially grown InSb NWs with WZ phase and even ZB twinning superlattice have been demonstrated and show the possibility of obtaining other crystal phase than ZB and crystal phase superlattices in NWs with high-Sb content.[48–50]

2.3 Core-shell structures

As was discussed in section 2.1, the presence of Sb adatoms on the NW sidewalls causes enhanced radial growth for III-As-Sb NWs as compared to the growth of III-As NWs. Due to different growth modes of radial vapor-solid and axial vapor-liquid-solid, it is expected that there exists a composition variation radially in the self-formed core-shell structure, especially considering the different diffusivity of As and Sb. Xu et al. [16] reported that during the growth of Au-catalyzed InAsSb nanowires, a conformal InAsSb shell with higher Sb content than the core was formed. This radial growth of self-formed InAsSb shell should follow the nucleation and step-flow mechanism proposed in the growth regime of the vapor-solid method.[17] However, it is not always true that the radial growth has a higher Sb content. Due to the polarity-driven 3-fold symmetry, similar to what was observed in the AlGaAs system [51,52], the self-catalyzed GaAsSb NWs can have a relatively inhomogeneous GaAsSb shell with a lower average Sb content and a homogeneous GaAsSb core of higher Sb content, as shown in figure 6.[19] This quite distinct variation of the Sb content in the self-formed core-shell structure is growth condition-dependent and should be specifically considered in relation to the catalyst composition and the specific growth window.[53]

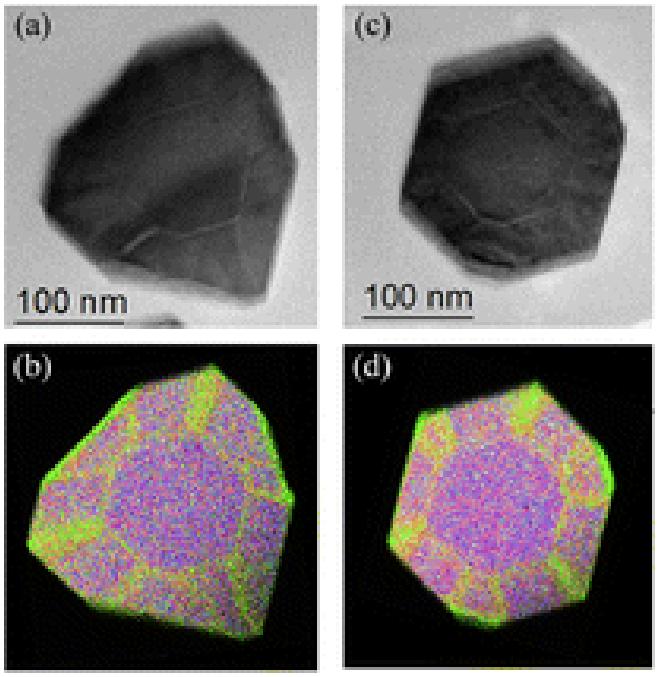

Figure 6. (a–d) Cross-section TEM image in the [-1-1-1] zone axis and associated energy dispersive X-ray spectroscopy (EDS) maps taken at the bottom (a,b) and top regions (c,d) of an MBE grown self-catalyzed core-shell GaAsSb NW. The composite EDS maps show the signal for As (green color), Ga (red color), and Sb (blue color); the yellow/green regions at apexes and interfaces are Sb-poor, with about 10% less Sb than in the violet regions. (Adapted with permission from [19]. Copyright 2014 American Chemical Society.).

In addition to the over growth-induced core-shell structure formation, a near-surface depletion of Sb in the radial direction of self-catalyzed GaAsSb NWs grown by MBE has been observed.[54,55] By making two electrical contacts to top and bottom sections, respectively, of a single GaAsSb NW, reproducible rectifying behavior has been observed for Sb molar fractions below 0.5.[44,54] This shows promise for applications based on single NW devices, e.g. photodetectors, without complex doping or post-growth fabrication. Low-frequency noise measurements have been performed on such a single NW device with self-induced compositional gradients, and the noise has been found to follow a typical 1/f behavior with the Hooge's noise parameter and an interface trap density of ~ 2.2×10^{-2} and ~ 2×10^{12} eV^{-1} cm^{-2}, respectively.[56]

In comparison to the self-formed core-shell structure, intentionally grown core-shell structures bring about new possibilities for fine tuning the composition in a wider range with better control. In self-catalyzed growth, the catalyst can be easily solidified by only supplying group-V flux, which further benefits radial growth without unwanted axial growth, in contrast to the Au-catalyzed growth. The schematic illustration of the growth of a GaAsSb shell over a GaAs NW core, can be seen in figure 7. Using this scheme, a wider range of Sb incorporation, up to an Sb molar fraction of 0.3, has been realized in self-catalyzed GaAs/GaAsSb core–shell NWs directly grown on Si(111) substrates by MBE, covering the miscibility gap of the GaAsSb ternary alloy.[57] In addition, a WZ GaAsSb shell can be formed by copying the core crystal phase, and this can help to realize the WZ crystal phase, which is challenging to achieve with significant amount of Sb used for the axial growth.[57,58] Efforts have been made using core-shell structured GaAsSb NWs to achieve optical emission in the telecom wavelength band, and photoluminescence (PL) emission at ~1.3 μm has been observed by tuning the growth temperature and V/III ratio for both GaAs/GaAsSb and GaAs/GaAsSbN systems.[59,60] By further growth of a double-shell configuration, the optical emission intensity can be further enhanced.[60]

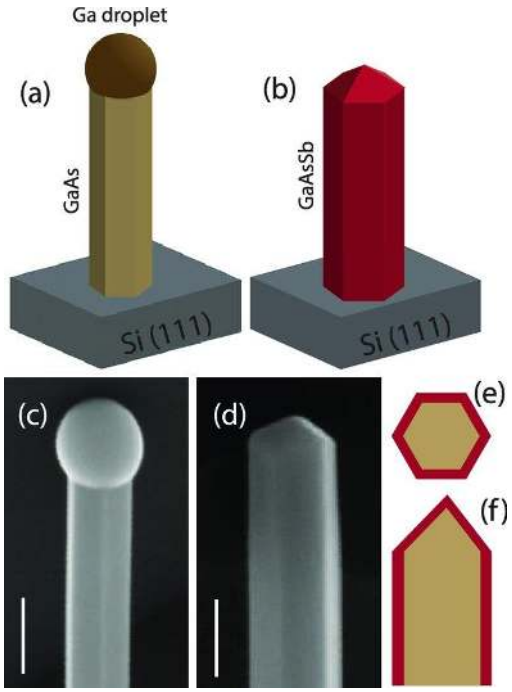

Figure 7. Schematic illustration of (a) a self-catalyzed GaAs core NW directly grown on Si(111) substrates. (b) A GaAs/$GaAs_x Sb_{1-x}$ core-shell NW where the $GaAs_x Sb_{1-x}$ shell is grown after a Ga-solidification process. Magnified SEM images of (c) a self-catalyzed GaAs NW directly grown on the Si substrate and (d) a GaAs/ $GaAs_x Sb_{1-x}$ core-shell NW. The scale bar for (c) and (d) is 100 nm. Cross sectional (e) top and (f) side schematic view of the GaAs/ $GaAs_x Sb_{1-x}$ core-shell NWs. (Reprinted with permission from [57]. Copyright 2013 IOP publishing.)

Other than the GaAs/GaAsSb core-shell structure, GaSb/InAsSb and GaAsSb/InAs systems have also attracted a lot of attention due to their interesting electrical behavior. An InAsSb shell grown over the GaSb NW core has been reported to lower the barrier for carrier injection and further enhance

the room temperature field-effect mobility from 42 for GaSb bare core to 200 $cm^2/(V \cdot s)$ with InAsSb shell at room temperature.[61] This further facilitated low-temperature quantum transport with quantum dots and large spin-orbit interaction in these materials.[62] Another interesting feature of these material systems is the controllability of intrinsic doping. Since nominally intrinsic InAs and GaSb NWs are unintentionally n-type and p-type semiconductors, respectively, the transport characteristics can be tuned by varying the composition and shell thickness and natural p-n junctions can be formed for infra-red applications.[63–65]

2.4 Bandgap tunability

The strong dependence of the III-As-Sb bandgap on the Sb content, which will be discussed in greater detail in section 3, opens up the possibility of tailoring the band alignment of NW heterostructures through precise compositional control for the purpose of a specific application. Due to an existing miscibility gap in the III-As-Sb material systems, it is thus both theoretically interesting and practically useful to explore the growth of III-As-Sb NWs in a wide compositional range.[66]

It is most convenient to tune the composition of III-As-Sb NWs by the Au-assisted growth method due to the wider growth window and stable Au catalyst particles. Sb nominal molar fraction from 0.08 to 0.75 has been demonstrated by directly growing InAsSb NWs on an InAs(111)B substrate using MOVPE.[53] It was found that the Sb content does not significantly vary with growth temperature between 435 and 480 °C, and the NW length decreases with increasing temperature, indicating that the axial growth rate is rather insensitive to Sb precursor flow whereas supersaturation has an important influence on the axial growth. In Au-catalyzed growth, the Sb content in the solid phase does not change with In precursor flow. Interestingly, there is a transition from Au-catalyzed growth to In-seeded growth with increasing the TMIn flow and for V/III ratios less than 50. This change from a Au-catalyzed mechanism to an In-catalyzed growth can help achieve high Sb contents, e.g. of the order of 0.75. [53]

There is a specific interest for tuning the bandgap of GaAsSb NWs in the near infrared to cover the wavelengths of 1.3 and 1.55 μm, which are in high demand for telecom applications. Self-catalyzed GaAsSb NW arrays have been grown using MBE with both high yield and good morphological uniformity.[31] The room-temperature PL demonstrates that the emission energy can be tuned from 1.422 to 1.219 eV by only adding Sb flux under the growth condition of GaAs NWs, which corresponds to Sb molar fraction of up to 10 %.[31] In comparison to the low-Sb content NW growth, which is compatible with the GaAs NW growth window, the growth of high-Sb content NWs is much more challenging for the self-catalyzed growth method. Growth of self-catalyzed $GaAs_{1-x}Sb_x$ NWs with Sb molar fraction x of 0.6 has been demonstrated directly on Si, but further increasing the Sb flux and reducing the As flux results in thin film morphology rather than NW growth, as shown in figure 8. This is attributed to a surfactant effect of the Sb atoms that impedes the successful formation of Ga catalyst droplets with preferential contact angle suitable for NW growth. To address this, Li et al. [44] grew a GaAs stem prior to the growth of a GaAsSb segment. This helps increase the contact angle of the catalyst and promotes axial NW growth under high-Sb content conditions, preventing the formation of a thin film-like morphology.

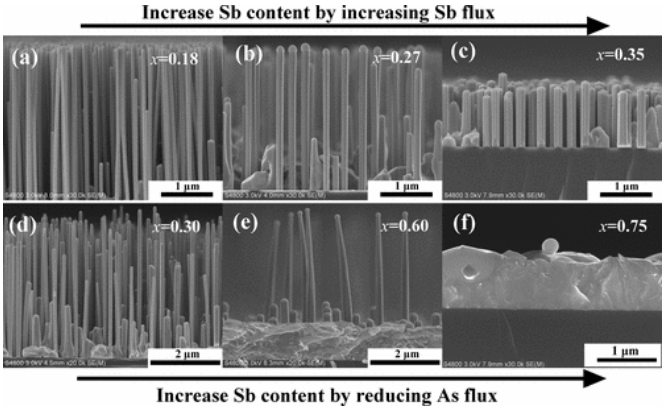

Figure 8. Side-view SEM images of self-catalyzed $GaAs_{1-x}Sb_x$ NWs grown on Si(111) substrates by MBE. (a–c) $GaAs_{1-x}Sb_x$ NWs with different Sb content were obtained by increasing the Sb flux and corresponding x values are 0.18, 0.27, and 0.35, respectively. (d–f) $GaAs_{1-x}Sb_x$ NWs with different Sb content were obtained by reducing the As flux and corresponding x values are 0.30, 0.60, and 0.75, respectively. (Adapted with permission from [44]. Copyright 2014 American Chemical Society.)

Another important measure for growing high-Sb content NWs with the self-catalyzed MBE growth method is decreasing the growth temperature in order to increase the supersaturation. As is shown in the GaAs-GaSb binary phase diagram, the solid-liquid equilibrium temperature drops with higher Sb content.[39] This suggests that the supersaturation inside the Ga catalyst will be reduced significantly with higher Sb flux. Since the supersaturation is the driving force for NW nucleation and growth, reducing the NW growth temperature would be a reasonable means to compensate for the supersaturation loss with Sb incorporation.[31,67] Both Li et al. [44] and Ahmad et al. [68] adopted a two-step growth method to facilitate Sb incorporation. At ~ 500 °C with high V/III flux ratio, axial GaAsSb NW segments were grown on GaAs NW stems with an Sb molar fraction of 0.93 by using background As pressure inside the MBE chamber. By exploring the growth windows, almost full composition range from GaSb to GaAs has been covered using self-catalyzed MBE growth.[44,68,69]

Instead of using a two-step growth strategy with higher Sb content, the formation of dilute-nitride GaAsSbN can tune the bandgap of ternary NWs with only minor nitrogen incorporation, as explained by the band anticrossing theory.[70] However, the areal density of NWs has been found to be reduced with higher Sb content. This is correlated with the consumption of the Ga flux into parasitic crystals formed on the substrate due to the presence of a higher group-V flux background. By measuring the PL at low temperature, the bandgap of dilute-nitride GaAsSbN has been found to be reduced to 1.1 eV.[71]

Due to random variations of the local environment during growth of self-assembled NWs, it is advantageous to have NW arrays with identical growth conditions for each NW. This is best achieved by growing ordered NW arrays with a well defined inter-NW separation, or pitch. Compared to binary NWs, an extra compositional variation could also exist for ternary NWs due to different elemental characteristics, e.g. the diffusion distance along the NW sidewalls. Sharma et al. [72] found that the re-emission from NW side-facets is dominant for small pitch morphology, and the surface re-emission from the substrate plays a major role in patterns with larger pitch, following a mass-continuity model developed by Gibson et al. [73]. This also correlates with a red shift of the PL emission for patterns with larger pitch length. Meanwhile, a lower contact angle will decrease the As collection efficiency, which takes place in patterns of small pitch length.[30,72] Considering that Sb has a longer diffusion distance than As, this leads to a higher Sb composition with smaller droplet contact angle, which has been confirmed by PL measurements on position controlled NW samples.[30]

2.5 Compositional characterization

To understand the growth and properties of III-As-Sb NWs as discussed above, compositional characterization is of significant importance. X-ray diffraction has been widely used for thin film characterization, and it is applied to evaluate the composition of III-As-Sb NWs in general as well. Although this macroscopic characterization technique is powerful and robust enough for the purposes of obtaining an overview, localized characterization is preferable due to the microscopic inhomogeneity of the NW composition.

Energy dispersive X-ray spectroscopy (EDS) in scanning transmission electron microscopy (STEM), i.e. STEM-EDS, is the most commonly used analytical tool for compositional characterization. It can provide localized compositional information by focusing the electron beam to a very tiny spot, usually around 1 nm, and scanning it over a targeted area. However, there are drawbacks. For example, the accuracy of k-factors used in the composition calculations is limited, the signal-to-noise ratio is often low and there are orientation-dependent effects that can influence the results [74]. The spatial resolution is also dependent on the TEM specimen thickness and overlap between regions with different Sb-content. By making a cross-section slice perpendicular to the axial axis from a III-As-Sb NW, the axial compositional variation can be identified. For example, using this technique on a core-shell GaAsSb NW, an Sb-poor shell over an Sb-rich core structure could be visualized, and for several axial positions, as depicted in figure 6(b) and (d).[19] More accurate but labor intensive than STEM-EDS is quantitative high-angle annular dark-field scanning transmission electron microscopy (HAADF-STEM). This quantitative method for evaluating the Sb distribution inside NW structures is based on normalizing image contrast relative to the incoming beam and comparing the results to simulations.[75,76] The better sensitivity and improved spatial resolution and accuracy allowed identifying an out-diffusion induced near-surface depletion of Sb in axial GaAsSb segments and GaAsSb NWs, which matches very well the developed diffusion model [46] and explains the rectifying behaviour from as-grown single NW devices.[54,55]

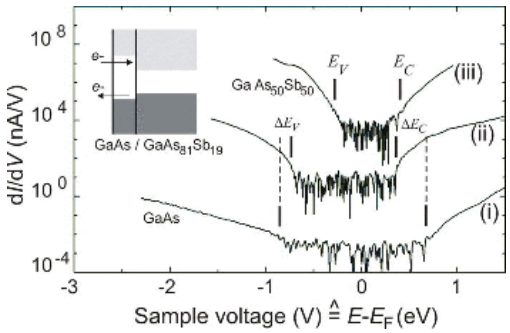

Figure 9. Tunneling spectra acquired on (i) the pure GaAs top segment and (ii) the shell surrounding the $GaAs_{0.81}Sb_{0.19}$ segment of a GaAs/$GaAs_{0.81}Sb_{0.19}$/GaAs heterostructured NW, as well as (iii) a $GaAs_{0.50}Sb_{0.50}$ NW. All spectra were acquired at 77 K with tunneling conditions of (i) 1.6 V, 0.8 nA, (ii) 1.6 V, 0.8 nA, and (iii) −1.0 V, 0.5 nA. Spectra (ii) and (iii) have been shifted for clarity. The conduction (E_C) and valence (E_V) band edges are indicated by vertical line segments, while ΔE_C and ΔE_V correspond to the band offsets between GaAs and the $GaAs_{0.81}Sb_{0.19}$ core. Inset: Energy band diagram of the radial GaAs/$GaAs_{0.81}Sb_{0.19}$ heterostructure, the arrows indicating the tunneling of electrons from or into the $GaAs_{0.81}Sb_{0.19}$ core through the GaAs shell. (Reprinted with permission from [77]. Copyright 2015 American Institute of Physics.)

STM and μ-Raman are also feasible tools for detailed investigation of the composition of III-As-Sb NWs. It has been found that the bright protrusions of atomic size in STM images from the InAsSb NW side facets, see e.g. figure 3(e) to (g), correlate with the presence of Sb, i.e. the Sb content, which matches the EDS measurement.[16] In addition, the tunnelling conductance, measured from the GaAsSb NW side facets, as shown in figure 9, has shown quantitative values for the

bandgap of the materials and even the band alignment in GaAsSb/GaAs core-shell and axial heterostructures. The bandgap and type-I band alignment agree well with the EDS analysis and are consistent with theoretical calculations.[77] In addition to STM characterization with atomic resolution and single atom precision at or close to the surface, Raman scattering can also provide localized compositional information, whose resolution depends on the laser spot size and penetration depth. Confocal μ-Raman measurements are capable of providing spatial information on the Sb composition along the axial direction of the NWs by correlating each shift of the optical phonon energy with the Sb content.[54,78] Beside the analytical techniques discussed so far, compositional analysis is also often based on optical analysis, and this will be discussed in detailed in the next chapter.

3. Optical properties of III-As-Sb

Both the optical characterization (by photo- or cathodoluminescence spectroscopy) and the successful realization of some of the most promising device applications (i.e. light emitters and absorbers) of III-As-Sb NWs require a detailed understanding of the relevant light emission and absorption processes in such NWs, which will be elucidated in this section. For a discussion of the III-As-Sb dielectric constant/indexof refraction dependence on the Sb content, we refer the reader to other works.[79,80] The transient carrier dynamics and photoconductivity due to photoexcited carriers can be further studied with optical techniques, such as Terahertz spectroscopy and Transient Absorption Spectroscopy which have lately attracted considerable attention in the nanowire research community [81–84]. However, so far no studies have come out where these techniques are applied to better understand III-Sb nanowire systems.

Light emission and absorption processes are first and foremost governed by the electronic band structure, including defect states within the band gap due to doping. In heterostructures, the energy band alignment between the constituent materials, quantum confinement, band bending effects and strain also play an important role. GaAs (1.52/1.43 eV), GaSb (0.813/0.726 eV), InAs (0.415/0.350 eV), and InSb (0.235/0.175 eV) are all direct band gap materials, with their respective band gap at low/room temperature indicated in brackets. Thus, III-As-Sb will also have a direct band gap. For the band gap width, it has been most common to rely on empirical expressions describing the variation of the composition-dependent band gap of thin films, usually at room temperature, as a function of the Sb molar fraction (x_{Sb}). Here, we cite the model for the unstrained GaAsSb band gap E_g at 300 K by Teissier et al. obtained by a quadratic fit to data points from multiple literature sources, valid for Sb molar fractions $x_{Sb} < 0.4$.[85]

$$E_g(x_{Sb}) = 1.43 - 2.24x_{Sb} + 1.97x_{Sb}^2. \quad (1)$$

It should be noted that this model is considered by the authors to be an improvement to the existing and commonly used model by Nahory et al. [86], which has the same functional shape, however different coefficients. The model by Teissier et al. was verified experimentally by Ahtapodov et al., using quantitative HAADF-STEM as an independent means for accurate determination of the Sb content.[55,87] A more recent theoretical work, covering the full range of Sb molar fractions and referencing experimental data for GaAsSb at room temperature has been published by Mezrag et al.[79] The band gap of InAsSb is commonly described by an equation similar to (1), taking the general shape:[88]

$$E_g(x_{Sb}) = E_g^{InSb}x_{Sb} + E_g^{InAs}(1 - x_{Sb}) - C x_{Sb}(1 - x_{Sb}) \quad (2)$$

The most frequently cited value for the bowing parameter C of 672 meV dates back to the paper by Fang et al. [89], although a more recent study by Svensson et al. [88] concludes that a value of 0.87 eV describes experimental data better. Interestingly, while the band gap reduction with increasing Sb molar fraction for As-rich III-As-Sb described by Eqs. (1-2) is approximately linear, the variation becomes non-monotonous at the Sb-rich end of the scale and the ternary compound attains a band gap width lower than both constituent binaries. This was reported by Nahory et al. [88] and Alberi et al. [90] for GaAsSb, and the situation is much the same with InAsSb (see figure 10), where the lowest attainable band-gap of any III-V material is achieved at an Sb molar fraction of 0.634 (145 meV at 10 K)[89].

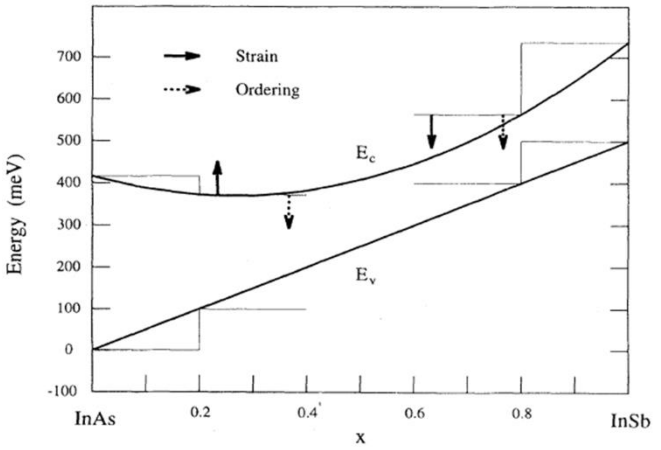

Figure 10. The model variation of the conduction and valence band edges of $InAs_{1-x}Sb_x$ in meV in relation to InAs as a function of the Sb molar fraction x. (Reprinted with permission from [92]. Copyright 1995 American Physics Society.)

There is a wide consensus that as Sb is added to GaAs/InAs, the III-As-Sb conduction band shifts downwards while the

band offset remains rather small. However, the dependence on Sb content is non-monotonous, as exemplified for InAsSb in figure 10. As reported by Johnson et al. for GaAsSb [91] and by several authors for InAsSb [92,93], as the Sb molar fraction increases, the conduction band offset passes through a maximum, after which it decreases until the cross-over point where it vanishes. This point is around a molar fraction of x = 0.34 and 0.5 for $GaAs_{1-x}Sb_x$[91] and $InAs_{1-x}Sb_x$[92], respectively. Meanwhile, the valence band offset is monotonously increasing with Sb content. Thus, at higher Sb molar fractions, the band alignment becomes type-II with the Sb bands lying higher (sometimes termed type-IIb).

As regards to both the band gap width of III-As-Sb and their energy band alignment to the associated III-As binaries, little NW-specific research has been done. However, the main results for bulk materials cited above have been found to describe well the optical properties of ZB NWs containing radial III-As-Sb shells or axial inserts. Still, in NWs, GaAs and InAs do also commonly occur in a WZ crystal structure, especially when Au-catalyzed growth is employed. The WZ phase has different symmetry and hence, generally speaking, different band gap and different band offsets to III-As-Sb materials. It has been established that the band alignment between ZB and WZ GaAs is type-II (with WZ band egdes lying higher) whereby the WZ band gap is approximately the same at low temperature, but possibly slightly larger at room temperature.[94] Both Vainorius et al. [95] and Ahtapodov et al. [87] arrive at values in the range 100-120 meV for the ZB/WZ GaAs band offsets at low temperature, and Ahtapodov et al. [87] observe only a small variation as temperature is increased up to 150 K. Thus, the heterojunction between WZ GaAs and ZB GaAsSb is type-II at low Sb concentration, and is expected to turn into type-I above a certain Sb molar fraction where the GaAsSb valence band rises above that of WZ GaAs. Due to the steep decrease of the (ZB) GaAsSb band gap with increasing Sb content, this transition is expected to occur at very low Sb molar fraction, which was estimated to be around 0.05 at cryogenic temperatures, based on refs.[85,87] For Sb-rich GaAsSb in strained heterostructures, the band alignment will become type-II again once the GaAsSb conduction band edge rises higher than that of WZ GaAs.

The band gap of WZ InAs is also higher than that of ZB InAs at low temperature, however by a relatively much larger margin as compared to GaAs. Möller et al. [96], report a band gap value of 488 meV at low temperature obtained by PL spectroscopy of WZ InAs NWs with relatively few stacking faults while Hjort et al. [42] have obtained a value of 390 meV at room temperature by combining STM on single NWs and DFT calculations, as compared to the corresponding ZB band gap of 350 meV. It is widely agreed that the band offsets between WZ and ZB InAs are similar to the GaAs case, i.e. the band alignment is type-II with the WZ band edges lying higher in energy. However and interestingly, Hjort et al. found that in practice, due to the inherent n-type doping of InAs, the conduction band edges in an actual crystal phase heterojunction are aligned, which places the WZ valence band edge below the ZB one, contrary to popular belief. The variation of the WZ InAs band gap and offsets to ZB InAs, excluding doping-related effects, means that, similar to the GaAs case, the heterojunction between WZ InAs and ZB InAsSb will be type-I through a significant part of the Sb molar fraction range, except below about 0.1 when the InAsSb valence band is still below that of WZ InAs, and above about 0.7 when the conduction band rises higher than that of WZ InAs. It is however unclear how this band alignment would be affected by unintentional n-type doping and the consequent Fermi level pinning between the two materials.

As both GaAs and InAs NWs can presently be grown in a nearly defect-free WZ crystal phase, and since the shell copies the crystal structure of the core, it is possible to fabricate core-shell NWs containing WZ III-As-Sb shells.[57] However, the band alignment in such a heterostructure is still a largely uncharted territory from an experimental point of view.

A further important feature of III-As-Sb NWs are the polarization properties of light absorption and emission. In part, these are governed by the energy band symmetry near the center of the Brillouin zone (i.e. at the Γ point) through the selection rules. Axial III-As-Sb segments exhibit a stable ZB crystal phase, which means that polarization along and perpendicular to the NW growth axis is dipole-allowed for both light emission and resonant absorption. In this case the preferential polarization for both light emission and resonant absorption, as well as non-resonant absorption, will be along the NW growth axis due to the dielectric mismatch effect between the high-index NW (e.g. n ~ 3.6 for GaAs) and its low-index surroundings (e.g. air, n = 1).[97] This is contrary to WZ materials (such as e.g. a III-As-Sb shell around a WZ NW core), where polarization directions along the crystallographic c-axis (which coincides with the growth axis) are forbidden.[98]

GaAs is notorious for the occurrence of defect-related surface states within the band gap, Fermi level pinning and strong non-radiative recombination of photoexcited carriers at unpassivated surfaces.[81,99] However, Alarcon-Llado et al. [78] reported that the addition of Sb boosts the luminescence intensity significantly and hence passivates the material surface to an extent. Still, surface passivation by fabricating a conformal radial shell of a wider-gap material is a common approach to improve the optical quality of semiconductor NWs and has been successfully applied also to III-As-Sb. Yuan et al. [100] have employed InP to passivate the GaAsSb NW core. Due to a surfactant effect that changes the surface energy of NW facets, a triangular shell over-growth was formed with predominant {112}A facets on the hexagonal NW geometry. A significant enhancement of the PL intensity

was observed with an InP shell. The PL lifetime of photoexcited carriers was also improved from 31 to 127 ps and 25 to 824 ps at room temperature and 10 K, respectively, indicating a significant reduction of the non-radiative recombination.[100] Ren et al. [31] used an AlGaAs shell and a GaAs cap to passivate the GaAsSb core. In a follow-up study by the same group which will be presented in more detail later in this review, GaAsSb-based superlattices in a GaAs-core NW, clad with an AlGaAs shell and GaAs cap were shown to exhibit optically excited lasing at record low thresholds for III-V NWs, indicating an efficient surface passivation in the studied structure.[4]

4. III-As-Sb based optoelectronic devices

Since epitaxially grown NWs can be monolithically integrated on the substrate without complex post-growth processing, e.g. wafer bonding, it is evident that NW-based devices, especially monolithically integrated on a III-V or Si platform, are viable candidates for various applications.[101–104] Based on the present level of understanding of the epitaxial growth, structural and optical properties of III-As-Sb NWs, discussed in the preceding, we will here elaborate on the state-of-the-art development of using epitaxially grown GaAsSb and InAsSb NWs as light detectors and emitters in the near- and mid-infrared wavelengths, and potentially into the far-infrared.

4.1 Photodetectors

NWs can exhibit strong light absorption once the diameter becomes comparable with the bandgap wavelength and external light can couple into waveguide modes of the NW. In addition, due to their (quasi) 1D geometry, NWs can form high-quality heterostructures accommodating for large lattice mismatch, resulting in a much better material quality than thin films. This should further enhance the performance of light absorbers, e.g. photodetectors. Through judicious tuning of the wire diameter by enhanced radial overgrowth, as discussed in section 2.3, Svensson et al. [105] showed that the absorption in InAs/InAsSb NWs can be increased by more than one order of magnitude at a specific wavelength compared to a thin planar film with the same amount of material. Due to enhanced coupling of light into the NW resonant modes, the absorption peak red-shifts for thicker NWs. Svensson et al. demonstrated a 20% cutoff wavelength of 5.7 μm at 5 K for $InAs_{0.38}Sb_{0.62}$-photodetectors, which highlights the potential of InAsSb-based NW photodetectors in the far-infrared.

For as-grown vertical NW devices, a position controlled NW array geometry is preferred due to easier device fabrication, less variation between individual NWs and better flexibility to tune the light trapping capability by modulating the interwire distance as compared to randomly grown NWs. A far-infrared photodetector based on an ordered InAsSb NW array has been grown by MBE on a Si(111) substrate with SiO_2 mask.[106] The array pattern was defined by using electron beam lithography, and the atomic force microscopy (AFM) image in figure 11(a) shows the etched holes in the oxide layer on the Si substrate. By using catalyst-free selective-area epitaxy, InAs/InAsSb NWs can be nucleated and grown from the holes on the oxide mask with good uniformity and high yield, as illustrated in figure 11(b) and (c). After growing a p-InAs segment for nucleation, the p-InAsSb/i-InAsSb/n-InAsSb structure, shown schematically in figure 11(d), has been grown axially to form an active medium in the array, and it exhibits an exceptionally low leakage current density of less than 2 mA/cm^2 at 300 K, as shown in figure 11(e). This value is almost two orders of magnitude lower than the best InAs(Sb) thin film-based photodiodes with leakage current densities around 100 mA/cm^2.[106]

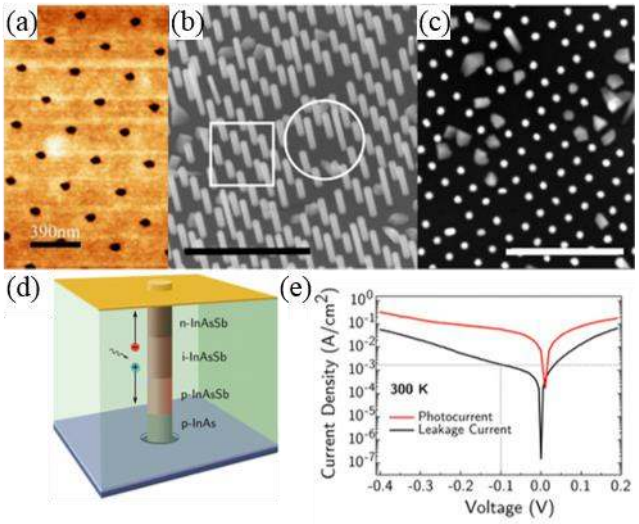

Figure 11. (a) AFM image of the etched holes in the oxide layer on the Si(111) substrate. (b) SEM image at 30° tilt of InAs/InAsSb NWs grown in the holes in the oxide layer. The square and circular outlines indicate regions of uniform and nonuniform growth, respectively. (c) Top-view SEM image of an array of InAs/InAsSb NWs with highly uniform NW diameter. (d) Schematic of a p–i–n InAsSb NW photodiode in the array. The NW consists of a 200 nm Be doped InAs stub followed by 500 nm Be doped InAsSb, 500 nm undoped InAsSb, and 500 nm Te doped InAsSb. The NW is encapsulated by cross-linked SU-8 with Ti/Au forming the top contact. (e) Semilog current–voltage characteristic of an $InAs_{0.93}Sb_{0.07}$ p–i–n photodiode at 300 K with a NW diameter of 80 nm and a length of 1.7 μm. The black and red plots show the leakage current and photocurrent density, respectively, for 200 contacted NWs. The scale bars for (a), (b) and (c) are 390 nm, 2 μm and 2 μm, respectively. (Adapted with permission from [106]. Copyright 2016 American Chemical Society.).

Efforts have also been made to enhance the absorption by growing densely packed InAsSb NW clusters that can act as a

collective photonic waveguide in order to compensate for the difficulty of growing NWs with hundreds of nm thickness, which is required for a photonic waveguide in the mid-infrared.[107] It has been found that the mid-IR light absorption of InAsSb NW clusters with 1.6 μm inter-cluster separation can be 200 times larger at the resonant wavelength of 5.6 μm than for NWs placed in an equidistant pattern. This significant enhancement should result from a collective mode formed by optically coupling neighboring NWs and the transmission can be strongly reduced based on a cluster size-wavelength dependency.[107]

Although achieving thick NWs for efficient mid-IR absorption is challenging for bottom-up growth synthesis, current catalyst-free selective-area epitaxy can achieve NWs suitable for short-wavelength IR (SWIR) absorption.[108] Recently, large diameter InAsSb NW arrays have been epitaxially grown on a Si(111) substrate using MBE. By tuning the period of the inter-wire distance on the hole mask, the diameter, length and composition of the NWs can be tuned accordingly. This results in different absorption of the SWIR light into the dominant HE_{11} mode of NW cavities in different arrays. By making a variety of arrays of different inter-wire separation on the same substrate in one single epitaxial growth, multispectral absorbance in SWIR photodetectors can be achieved, which provides an example solution for NW-based multispectral IR photodetectors and sensors.[108]

Most recently, as-grown InAsSb nanowire array photodetector has been integrated with plasmonic metal grating, which enhances the absorption of light with long wavelength using relatively thin and small volume NWs. With excellent surface passivation using Al_2O_3 by atomic layer deposition, the device with optimized pitch and diameter shows room-temperature spectral response with MWIR detection signatures up to 3.4 μm.[109] These array devices have the great potential to be integrated even with Si platform.[110]

Compared to as-grown NW-based photodetectors, single NW devices have much smaller dimensions, which attracts great attention for high-resolution sensing applications. Both self-induced rectifying GaAsSb [54] and non-rectifying $GaAs_{0.56}Sb_{0.44}$ NWs [111] have been demonstrated as single NW infrared photodetectors operating at room temperature. The self-induced rectifying NWs exhibit a state-of-the-art photoresponsivity of around 1463 A/W under reverse bias (-3 V) and under an illumination intensity of 20.7 mW/cm^2. This value is 48000 and 2500 times higher than that for a GaAs NW photodetector and for a GaAs/AlGaAs core–shell NW photodetector, respectively, which was attributed to the higher local electric field for a reverse biased Schottky barrier.[54] By further increasing the Sb content, the self-induced rectifying behavior vanishes [44], and single NW photodetectors using MOVPE grown $GaAs_{0.56}Sb_{0.44}$ NWs with good ohmic contact have been developed.[111] A field-effect transistor has also been made using MOVPE grown $GaAs_{0.56}Sb_{0.44}$ NWs on p+-type Si substrate with 300 nm thermal SiO_2 dielectric at the surface.[111] The peak field-effect mobility was shown to be ~ 12 cm^2/(V·s) with a calculated hole carrier concentration of 3.2×10^{17} cm^{-3}.[111] Temperature-dependent measurements were performed to understand the photocurrent properties of the NW photodetector. A decreased photocurrent was observed once the temperature was reduced, which indicates that a large number of trap centers and a high density of surface states exist. At room temperature, the trapped carriers were thermally excited and the NW photodetector showed a broadband infrared photo response from 1.1 to 1.66 μm with a responsivity of 2.37 and 1.44 A·W^{-1} at the wavelength of 1.3 and 1.55 μm, respectively.[111]

4.2 Light emitters

Apart from efficient light absorbers, III-As-Sb NWs can also act as efficient, miniaturized light emitters operating in the infrared with practical application importance, e.g. for optical communications and gas sensing.

As a direct bandgap material, covering the wavelength range between 1.3 and 1.55 μm, GaAsSb has been considered for applications in optical telecommunications. By utilizing quantum confinement effects, the emission efficiency can be significantly enhanced. GaAsSb/AlGaAs core-shell heterostructures have been grown by MOVPE, and shown to reach internal quantum efficiencies as high as 90%.[112] Under pulsed optical excitation, the spontaneous emission can be coupled to the TE_{01} mode of the NW Fabry–Perot cavity, enabling strong amplified spontaneous emission at room temperature.[112]

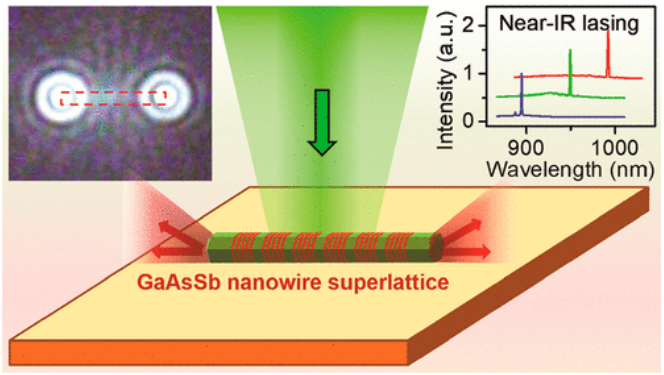

Figure 12. Schematic of an optically pumped single NW laser with GaAsSb-based superlattice gain structure. The left inset shows the optical image of the lasing NW laser and the right inset presents a wide range of lasing wavelengths from the lasers of different Sb composition profile. (Reprinted with permission from [4]. Copyright 2018 American Chemical Society.)

Apart from radial heterostructures, efforts have also been made towards efficient lasing emission using axial structures

with quantum confinement. A NW consisting of GaAsSb-based multiple superlattices, schematically depicted in figure 12, each superlattice containing ten GaAsSb-rich quantum wells, has been grown on a Si(111) substrate by a position-controlled self-catalyzed method.[4] The compositional analysis shows that the GaAsSb-based quantum wells are quite consistent from the second superlattice onwards, which results in a uniform cathodoluminescence emission from the GaAsSb quantum wells along the NW. Optically pumped single-mode lasing (optical image shown in the left inset in figure. 12) was observed from 890 to 990 nm (spectra shown in right inset of figure 12) by adjusting the Sb content of the NW quantum wells, delivering a lasing quality (Q) factor as high as 1250 with a high characteristic temperature of 129 K. Moreover, by increasing the Sb content, which results in deeper quantum wells in the superlattice, the lasing threshold was reduced from ~12 to ~6 kW/cm^2 (75 μJ/cm^2 per pulse), which is among the lowest values for any III-V nanolaser reported so far.

Compared to other infrared light emitters, mid-infrared NW emitters suffer from strong non-radiative Auger and surface recombination, which requires the incorporation of low-dimensional structures with enhanced efficiency.[113] Type-II InAsSb/InAs multi quantum wells (MQWs) have been integrated inside InAs NWs using catalyst-free selective area epitaxy on a Si(111) substrate.[114,115] These InAsSb MQWs exhibit mid-infrared emission up to room temperature. The conical QWs can efficiently confine the electron-hole recombination, suppressing the surface non-radiative recombination. In comparison to bare InAsSb NWs, the emission from InAsSb MQWs presents significant blue shift with increased excitation power, and the PL intensity at low temperature is more than four times higher. Further benefiting from the specific type-II band alignment, the QWs can spatially separate the electrons and holes, which helps to suppress the Auger recombination. By stronger excitation, the overlap of the electron and hole wavefunctions was improved from approximately 40% to 70%, while the suppression of the Auger recombination remains efficient, enabling PL emission up to room temperature.[114]

We should note here that there is still no report of a robust III-As-Sb NW-based laser device with an efficient p-n junction. This certainly requires more detailed studies on the doping behaviour in these ternary NWs, linking the current understanding on morphologies, crystal phases and band structures control.[116] In addition, the optical emission in these ternaries suffers from a peak broadening effect. This phenomenon mostly comes from a compositional fluctuation and should be suppressed for high-performance lasers and photodetectors.[31,44,117]

5. Summary

In this review, the state-of-the-art of III-As-Sb, i.e. GaAsSb and InAsSb, NW growth and properties has been discussed in detail. It has been demonstrated that these ternary NWs can be epitaxially grown on a variety of substrates with the flexibility to tune the bandgap, covering a wide range of important wavelengths. The incorporation of Sb into InAs and GaAs NWs brings about new phenomena that are crucial and advantageous for designing high-efficiency optoelectronic devices, such as photodetectors and optically pumped lasers in both near-infrared and mid-infrared wavelength ranges.

Acknowledgements

This work is supported by the NANO2021 (grant no. 239206) programs of the Research Council of Norway. The Research Council of Norway is also acknowledged for the support to the Norwegian PhD Network on Nanotechnology for Microsystems (grant no. FORSKERSKOLER-221860).

References

[1] Aberg I, Vescovi G, Asoli D, Naseem U, Gilboy J P, Sundvall C, Dahlgren A, Svensson K E, Anttu N, Bjork M T and Samuelson L 2016 A GaAs Nanowire Array Solar Cell With 15.3% Efficiency at 1 Sun *IEEE J. Photovoltaics* **6** 185–90

[2] Mourik V, Zuo K, Frolov S M, Plissard S R, Bakkers E P A M and Kouwenhoven L P 2012 Signatures of Majorana Fermions in Hybrid Superconductor-Semiconductor Nanowire Devices *Science.* **336** 1003–7

[3] Sestoft J E, Kanne T, Gejl A N, von Soosten M, Yodh J S, Sherman D, Tarasinski B, Wimmer M, Johnson E, Deng M, Nygård J, Jespersen T S, Marcus C M and Krogstrup P 2018 Engineering hybrid epitaxial InAsSb/Al nanowires for stronger topological protection *Phys. Rev. Mater.* **2** 044202

[4] Ren D, Ahtapodov L, Nilsen J S, Yang J, Gustafsson A, Huh J, Conibeer G J, van Helvoort A T J, Fimland B-O and Weman H 2018 Single-Mode Near-Infrared Lasing in a GaAsSb-Based Nanowire Superlattice at Room Temperature *Nano Lett.* **18** 2304–10

[5] Li J, Wang D and R. LaPierre R 2012 *Advances in III-V Semiconductor Nanowires and Nanodevices* (BENTHAM SCIENCE PUBLISHERS)

[6] Mattias Borg B and Wernersson L-E 2013 Synthesis and properties of antimonide nanowires *Nanotechnology* **24** 202001

[7] Dheeraj D L, Patriarche G, Largeau L, Zhou H L, van Helvoort A T J, Glas F, Harmand J C, Fimland B O and Weman H 2008 Zinc blende GaAsSb nanowires grown by molecular beam epitaxy *Nanotechnology* **19** 275605

[8] Dheeraj D L, Patriarche G, Zhou H, Hoang T B, Moses A F, Grønsberg S, van Helvoort A T J, Fimland B-O and Weman H 2008 Growth and Characterization of Wurtzite GaAs Nanowires with Defect-Free Zinc Blende GaAsSb Inserts *Nano Lett.* **8** 4459–63

[9] Borg B M, Dick K A, Eymery J and Wernersson L-E 2011 Enhanced Sb incorporation in InAsSb nanowires grown by metalorganic vapor phase epitaxy *Appl. Phys. Lett.* **98** 113104

[10] Plissard S, Dick K A, Wallart X and Caroff P 2010 Gold-free GaAs/GaAsSb heterostructure nanowires grown on silicon *Appl. Phys. Lett.* **96** 121901

[11] Harmand J C, Patriarche G, Péré-Laperne N, Mérat-Combes

M-N, Travers L and Glas F 2005 Analysis of vapor-liquid-solid mechanism in Au-assisted GaAs nanowire growth *Appl. Phys. Lett.* **87** 203101

[12] Motohisa J, Noborisaka J, Takeda J, Inari M and Fukui T 2004 Catalyst-free selective-area MOVPE of semiconductor nanowires on (111)B oriented substrates *J. Cryst. Growth* **272** 180–5

[13] Dick K A, Deppert K, Samuelson L and Seifert W 2007 InAs nanowires grown by MOVPE *J. Cryst. Growth* **298** 631–4

[14] Colombo C, Spirkoska D, Frimmer M, Abstreiter G and Fontcuberta i Morral A 2008 Ga-assisted catalyst-free growth mechanism of GaAs nanowires by molecular beam epitaxy *Phys. Rev. B* **77** 155326

[15] Plissard S, Dick K A, Larrieu G, Godey S, Addad A, Wallart X and Caroff P 2010 Gold-free growth of GaAs nanowires on silicon: arrays and polytypism *Nanotechnology* **21** 385602

[16] Xu T, Dick K A, Plissard S, Nguyen T H, Makoudi Y, Berthe M, Nys J-P, Wallart X, Grandidier B and Caroff P 2012 Faceting, composition and crystal phase evolution in III–V antimonide nanowire heterostructures revealed by combining microscopy techniques *Nanotechnology* **23** 095702

[17] Ercolani D, Gemmi M, Nasi L, Rossi F, Pea M, Li A, Salviati G, Beltram F and Sorba L 2012 Growth of InAs/InAsSb heterostructured nanowires *Nanotechnology* **23** 115606

[18] Yuan X, Yang J, He J, Tan H H and Jagadish C 2018 Role of surface energy in nanowire growth *J. Phys. D. Appl. Phys.* **51** 283002

[19] Conesa-Boj S, Kriegner D, Han X-L, Plissard S, Wallart X, Stangl J, Fontcuberta i Morral A and Caroff P 2014 Gold-Free Ternary III–V Antimonide Nanowire Arrays on Silicon: Twin-Free down to the First Bilayer *Nano Lett.* **14** 326–32

[20] Du W-N, Yang X-G, Wang X-Y, Pan H-Y, Ji H-M, Luo S, Yang T and Wang Z-G 2014 The self-seeded growth of InAsSb nanowires on silicon by metal-organic vapor phase epitaxy *J. Cryst. Growth* **396** 33–7

[21] Anyebe E A, Rajpalke M K, Veal T D, Jin C J, Wang Z M and Zhuang Q D 2015 Surfactant effect of antimony addition to the morphology of self-catalyzed $InAs_{1-x}Sb_x$ nanowires *Nano Res.* **8** 1309–19

[22] Du W, Yang X, Pan H, Wang X, Ji H, Luo S, Ji X, Wang Z and Yang T 2015 Two Different Growth Mechanisms for Au-Free InAsSb Nanowires Grown on Si Substrate *Cryst. Growth Des.* **15** 2413–8

[23] Potts H, Friedl M, Amaduzzi F, Tang K, Tütüncüoglu G, Matteini F, Alarcon Lladó E, McIntyre P C and Fontcuberta i Morral A 2016 From Twinning to Pure Zincblende Catalyst-Free InAs(Sb) Nanowires *Nano Lett.* **16** 637–43

[24] Farrell A C, Lee W-J, Senanayake P, Haddad M A, Prikhodko S V. and Huffaker D L 2015 High-Quality InAsSb Nanowires Grown by Catalyst-Free Selective-Area Metal–Organic Chemical Vapor Deposition *Nano Lett.* **15** 6614–9

[25] Ren D, Farrell A C and Huffaker D L 2017 Selective-area InAsSb Nanowires on InP for 3 – 5 μm Mid-wavelength Infrared Optoelectronics *MRS Adv.* **2** 3565–70

[26] Yang X, Du W, Ji X, Zhang X and Yang T 2018 Defect-free InAsSb nanowire arrays on Si substrates grown by selective-area metal–organic chemical vapor deposition *Nanotechnology* **29** 405601

[27] Du W, Yang X, Pan H, Ji X, Ji H, Luo S, Zhang X, Wang Z and Yang T 2016 Controlled-Direction Growth of Planar InAsSb Nanowires on Si Substrates without Foreign Catalysts *Nano Lett.* **16** 877–82

[28] Anyebe E A, Sanchez A M, Hindmarsh S, Chen X, Shao J, Rajpalke M K, Veal T D, Robinson B J, Kolosov O, Anderson F, Sundaram R, Wang Z M, Falko V and Zhuang Q 2015 Realization of Vertically Aligned, Ultrahigh Aspect Ratio InAsSb Nanowires on Graphite *Nano Lett.* **15** 4348–55

[29] Ren D, Høiaas I M, Reinertsen J F, Dheeraj D L, Munshi A M, Kim D-C, Weman H and Fimland B-O 2016 Growth optimization for self-catalyzed GaAs-based nanowires on metal-induced crystallized amorphous substrate *J. Vac. Sci. Technol. B, Nanotechnol. Microelectron. Mater. Process. Meas. Phenom.* **34** 02L117

[30] Ren D, Huh J, Dheeraj D L, Weman H and Fimland B-O 2016 Influence of pitch on the morphology and luminescence properties of self-catalyzed GaAsSb nanowire arrays *Appl. Phys. Lett.* **109** 243102

[31] Ren D, Dheeraj D L, Jin C, Nilsen J S, Huh J, Reinertsen J F, Munshi A M, Gustafsson A, van Helvoort A T J, Weman H and Fimland B-O 2016 New Insights into the Origins of Sb-Induced Effects on Self-Catalyzed GaAsSb Nanowire Arrays *Nano Lett.* **16** 1201–9

[32] Yuan X, Caroff P, Wong-Leung J, Fu L, Tan H H and Jagadish C 2015 Tunable Polarity in a III-V Nanowire by Droplet Wetting and Surface Energy Engineering *Adv. Mater.* **27** 6096–103

[33] Dick K A, Caroff P, Bolinsson J, Messing M E, Johansson J, Deppert K, Wallenberg L R and Samuelson L 2010 Control of III–V nanowire crystal structure by growth parameter tuning *Semicond. Sci. Technol.* **25** 024009

[34] Glas F, Harmand J-C and Patriarche G 2007 Why Does Wurtzite Form in Nanowires of III-V Zinc Blende Semiconductors? *Phys. Rev. Lett.* **99** 146101

[35] Jacobsson D, Panciera F, Tersoff J, Reuter M C, Lehmann S, Hofmann S, Dick K A and Ross F M 2016 Interface dynamics and crystal phase switching in GaAs nanowires *Nature* **531** 317–22

[36] Harmand J-C, Patriarche G, Glas F, Panciera F, Florea I, Maurice J-L, Travers L and Ollivier Y 2018 Atomic Step Flow on a Nanofacet *Phys. Rev. Lett.* **121** 166101

[37] Algra R E, Verheijen M A, Feiner L-F, Immink G G W, Enckevort W J P van, Vlieg E and Bakkers E P A M 2011 The role of surface energies and chemical potential during nanowire growth. *Nano Lett.* **11** 1259–64

[38] Li J-B, Zhang W, Li C and Du Z 1998 A thermodynamic assessment of the Ga-As-Sb system *J. Phase Equilibria* **19** 466–72

[39] Panish M B and Ilegems M 1972 Phase equilibria in ternary III–V systems *Prog. Solid State Chem.* **7** 39–83

[40] Ghalamestani S G, Ek M, Ghasemi M, Caroff P, Johansson J and Dick K A 2014 Morphology and composition controlled $Ga_xIn_{1-x}Sb$ nanowires: understanding ternary antimonide growth *Nanoscale* **6** 1086–92

[41] Ghasemi M and Johansson J 2017 Phase diagrams for understanding gold-seeded growth of GaAs and InAs nanowires *J. Phys. D. Appl. Phys.* **50** 134002

[42] Hjort M, Lehmann S, Knutsson J, Zakharov A A, Du Y A, Sakong S, Timm R, Nylund G, Lundgren E, Kratzer P, Dick K A and Mikkelsen A 2014 Electronic and Structural Differences between Wurtzite and Zinc Blende InAs Nanowire Surfaces: Experiment and Theory *ACS Nano* **8** 12346–55

[43] Yan W, Qu Y, Gupta T Das, Darga A, Nguyên D T, Page A G, Rossi M, Ceriotti M and Sorin F 2017 Semiconducting Nanowire-Based Optoelectronic Fibers *Adv. Mater.* **29** 1700681

[44] Li L, Pan D, Xue Y, Wang X, Lin M, Su D, Zhang Q, Yu X, So H, Wei D, Sun B, Tan P, Pan A and Zhao J 2017 Near Full-Composition-Range High-Quality $GaAs_{1-x}Sb_x$ Nanowires

Grown by Molecular-Beam Epitaxy *Nano Lett.* **17** 622–30
[45] Zhuang Q D, Anyebe E A, Chen R, Liu H, Sanchez A M, Rajpalke M K, Veal T D, Wang Z M, Huang Y Z and Sun H D 2015 Sb-Induced Phase Control of InAsSb Nanowires Grown by Molecular Beam Epitaxy *Nano Lett.* **15** 1109–16
[46] Ba Hoang T, Moses A F, Ahtapodov L, Zhou H, Dheeraj D L, van Helvoort A T J, Fimland B-O and Weman H 2010 Engineering Parallel and Perpendicular Polarized Photoluminescence from a Single Semiconductor Nanowire by Crystal Phase Control *Nano Lett.* **10** 2927–33
[47] Munshi A M, Dheeraj D L, Todorovic J, van Helvoort A T J, Weman H and Fimland B-O 2013 Crystal phase engineering in self-catalyzed GaAs and GaAs/GaAsSb nanowires grown on Si(111) *J. Cryst. Growth* **372** 163–9
[48] Gorji Ghalamestani S, Lehmann S and Dick K A 2016 Can antimonide-based nanowires form wurtzite crystal structure? *Nanoscale* **8** 2778–86
[49] Yuan X, Guo Y, Caroff P, He J, Tan H H and Jagadish C 2017 Dopant-Free Twinning Superlattice Formation in InSb and InP Nanowires *Phys. status solidi - Rapid Res. Lett.* **11** 1700310
[50] Qian Y and Yang Q 2017 Straight Indium Antimonide Nanowires with Twinning Superlattices via a Solution Route *Nano Lett.* **17** 7183–90
[51] Zheng C, Wong-Leung J, Gao Q, Tan H H, Jagadish C and Etheridge J 2013 Polarity-driven 3-fold symmetry of GaAs/AlGaAs core multishell nanowires. *Nano Lett.* **13** 3742–8
[52] Kauko H, Zheng C L, Zhu Y, Glanvill S, Dwyer C, Munshi A M, Fimland B O, van Helvoort A T J and Etheridge J 2013 Compositional analysis of GaAs/AlGaAs heterostructures using quantitative scanning transmission electron microscopy *Appl. Phys. Lett.* **103** 232111
[53] Namazi L, Ghalamestani S G, Lehmann S, Zamani R R and Dick K A 2017 Direct nucleation, morphology and compositional tuning of $InAs_{1-x}Sb_x$ nanowires on InAs (111) B substrates *Nanotechnology* **28** 165601
[54] Huh J, Yun H, Kim D-C, Munshi A M, Dheeraj D L, Kauko H, van Helvoort A T J, Lee S, Fimland B-O and Weman H 2015 Rectifying Single GaAsSb Nanowire Devices Based on Self-Induced Compositional Gradients *Nano Lett.* **15** 3709–15
[55] Kauko H, Fimland B O, Grieb T, Munshi A M, Müller K, Rosenauer A and van Helvoort A T J 2014 Near-surface depletion of antimony during the growth of GaAsSb and GaAs/GaAsSb nanowires *J. Appl. Phys.* **116** 144303
[56] Huh J, Kim D-C, Munshi A M, Dheeraj D L, Jang D, Kim G-T, Fimland B-O and Weman H 2016 Low frequency noise in single GaAsSb nanowires with self-induced compositional gradients *Nanotechnology* **27** 385703
[57] Ghalamestani S G, Mazid Munshi A, Dheeraj D L, Fimland B-O, Weman H and Dick K A 2013 Self-catalyzed MBE grown $GaAs/GaAs_xSb_{1-x}$ core–shell nanowires in ZB and WZ crystal structures *Nanotechnology* **24** 405601
[58] Zhou C, Zheng K, Chen P-P, Matsumura S, Lu W and Zou J 2018 Crystal-phase control of GaAs–GaAsSb core–shell/axial nanowire heterostructures by a two-step growth method *J. Mater. Chem. C* **6** 6726–32
[59] Kasanaboina P K, Ojha S K, Sami S U, Reynolds C L, Liu Y and Iyer S 2015 Bandgap tuning of GaAs/GaAsSb core-shell nanowires grown by molecular beam epitaxy *Semicond. Sci. Technol.* **30** 105036
[60] Kasanaboina P K, Ahmad E, Li J, Reynolds C L, Liu Y and Iyer S 2015 Self-catalyzed growth of dilute nitride GaAs/GaAsSbN/GaAs core-shell nanowires by molecular beam epitaxy *Appl. Phys. Lett.* **107** 103111
[61] Ganjipour B, Sepehri S, Dey A W, Tizno O, Borg B M, Dick K A, Samuelson L, Wernersson L-E and Thelander C 2014 Electrical properties of GaSb/InAsSb core/shell nanowires *Nanotechnology* **25** 425201
[62] Ganjipour B, Leijnse M, Samuelson L, Xu H Q and Thelander C 2015 Transport studies of electron-hole and spin-orbit interaction in GaSb/InAsSb core-shell nanowire quantum dots *Phys. Rev. B* **91** 161301
[63] Ganjipour B, Ek M, Mattias Borg B, Dick K A, Pistol M-E, Wernersson L-E and Thelander C 2012 Carrier control and transport modulation in GaSb/InAsSb core/shell nanowires *Appl. Phys. Lett.* **101** 103501
[64] Ji X, Yang X, Du W, Pan H and Yang T 2016 Selective-Area MOCVD Growth and Carrier-Transport-Type Control of InAs(Sb)/GaSb Core–Shell Nanowires *Nano Lett.* **16** 7580–7
[65] Li L, Pan D, So H, Wang X, Yu Z and Zhao J 2017 GaAsSb/InAs core-shell nanowires grown by molecular-beam epitaxy *J. Alloys Compd.* **724** 659–65
[66] Müller E K and Richards J L 1964 Miscibility of III-V Semiconductors Studied by Flash Evaporation *J. Appl. Phys.* **35** 1233–41
[67] Glas F, Ramdani M R, Patriarche G and Harmand J-C 2013 Predictive modeling of self-catalyzed III-V nanowire growth *Phys. Rev. B* **88** 195304
[68] Ahmad E, Karim M R, Hafiz S Bin, Reynolds C L, Liu Y and Iyer S 2017 A Two-Step Growth Pathway for High Sb Incorporation in GaAsSb Nanowires in the Telecommunication Wavelength Range *Sci. Rep.* **7** 10111
[69] Deshmukh P, Sharma M, Nalamati S, Reynolds C L, Liu Y and Iyer S 2018 Molecular beam epitaxial growth of high quality Ga-catalyzed $GaAs_{1-x}Sb_x$ ($x > 0.8$) nanowires on Si (111) with photoluminescence emission reaching 1.7 μm *Semicond. Sci. Technol.* **33** 125007
[70] Lin Y-T, Ma T-C, Chen T-Y and Lin H-H 2008 Energy gap reduction in dilute nitride GaAsSbN *Appl. Phys. Lett.* **93** 171914
[71] Sharma M, Deshmukh P, Kasanaboina P, Reynolds C L, Liu Y and Iyer S 2017 Growth of defect-free GaAsSbN axial nanowires via self-catalyzed molecular beam epitaxy *Semicond. Sci. Technol.* **32** 125003
[72] Sharma M, Karim M R, Kasanaboina P, Li J and Iyer S 2017 Pitch-Induced Bandgap Tuning in Self-Catalyzed Growth of Patterned GaAsSb Axial and GaAs/GaAsSb Core–Shell Nanowires Using Molecular Beam Epitaxy *Cryst. Growth Des.* **17** 730–7
[73] Gibson S J and LaPierre R R 2014 Model of patterned self-assisted nanowire growth *Nanotechnology* **25** 415304
[74] Williams, David B., Carter C B 2009 *Transmission Electron Microscopy*
[75] Kauko H, Bjørge R, Holmestad R and van Helvoort A T J 2012 Quantitative HAADF-STEM on heterostructured GaAs nanowires *J. Phys. Conf. Ser.* **371** 012056
[76] Kauko H, Grieb T, Bjørge R, Schowalter M, Munshi A M, Weman H, Rosenauer A and van Helvoort A T J 2013 Compositional characterization of GaAs/GaAsSb nanowires by quantitative HAADF-STEM *Micron* **44** 254–60
[77] Xu T, Wei M J, Capiod P, Díaz Álvarez A, Han X L, Troadec D, Nys J P, Berthe M, Lefebvre I, Patriarche G, Plissard S R, Caroff P, Ebert P and Grandidier B 2015 Type I band alignment in GaAs 81 Sb 19 /GaAs core-shell nanowires *Appl. Phys. Lett.* **107** 112102
[78] Alarcón-Lladó E, Conesa-Boj S, Wallart X, Caroff P and Fontcuberta i Morral A 2013 Raman spectroscopy of self-catalyzed GaAs 1− x Sb x nanowires grown on silicon

Nanotechnology **24** 405707
[79] Mezrag F, Aouina N Y and Bouarissa N 2006 Optoelectronic and dielectric properties of $GaAs_xSb_{1-x}$ ternary alloys *J. Mater. Sci.* **41** 5323–8
[80] Paskov P P 1997 Refractive indices of InSb, InAs, GaSb, $InAs_xSb_{1-x}$, and $In_{1-x}Ga_xSb$: Effects of free carriers *J. Appl. Phys.* **81** 1890–8
[81] Joyce H J, Docherty C J, Gao Q, Tan H H, Jagadish C, Lloyd-Hughes J, Herz L M and Johnston M B 2013 Electronic properties of GaAs, InAs and InP nanowires studied by terahertz spectroscopy *Nanotechnology* **24** 214006
[82] Joyce H J, Baig S A, Parkinson P, Davies C L, Boland J L, Tan H H, Jagadish C, Herz L M and Johnston M B 2017 The influence of surfaces on the transient terahertz conductivity and electron mobility of GaAs nanowires *J. Phys. D. Appl. Phys.* **50** 224001
[83] Yan W, Burgos-Caminal A, Das Gupta T, Moser J-E and Sorin F 2018 Direct Synthesis of Selenium Nanowire Mesh on a Solid Substrate and Insights into Ultrafast Photocarrier Dynamics *J. Phys. Chem. C* **122** 25134–41
[84] Joyce H J, Wong-Leung J, Yong C-K, Docherty C J, Paiman S, Gao Q, Tan H H, Jagadish C, Lloyd-Hughes J, Herz L M and Johnston M B 2012 Ultralow Surface Recombination Velocity in InP Nanowires Probed by Terahertz Spectroscopy *Nano Lett.* **12** 5325–30
[85] Teissier R, Sicault D, Harmand J C, Ungaro G, Le Roux G and Largeau L 2001 Temperature-dependent valence band offset and band-gap energies of pseudomorphic GaAsSb on GaAs *J. Appl. Phys.* **89** 5473
[86] Nahory R E, Pollack M A and Abrokwah J K 1977 Threshold characteristics and extended wavelength operation of $GaAs_{1-x}Sb_x$ / $Al_yGa_{1-y}As_{1-x}Sb_x$ double-heterostructure lasers *J. Appl. Phys.* **48** 3988–90
[87] Ahtapodov L, Kauko H, Munshi A M, Fimland B O, van Helvoort A T J and Weman H 2017 Determination of GaAs zinc blende/wurtzite band offsets utilizing GaAs nanowires with an axial GaAsSb insert *J. Appl. Phys.* **122** 245102
[88] Svensson S P, Sarney W L, Hier H, Lin Y, Wang D, Donetsky D, Shterengas L, Kipshidze G and Belenky G 2012 Band gap of $InAs_{1-x}Sb_x$ with native lattice constant *Phys. Rev. B* **86** 245205
[89] Fang Z M, Ma K Y, Jaw D H, Cohen R M and Stringfellow G B 1990 Photoluminescence of InSb, InAs, and InAsSb grown by organometallic vapor phase epitaxy *J. Appl. Phys.* **67** 7034–9
[90] Alberi K, Wu J, Walukiewicz W, Yu K M, Dubon O D, Watkins S P, Wang C X, Liu X, Cho Y-J and Furdyna J 2007 Valence-band anticrossing in mismatched III-V semiconductor alloys *Phys. Rev. B* **75** 045203
[91] Johnson S R, Guo C Z, Chaparro S, Sadofyev Y G, Wang J, Cao Y, Samal N, Xu J, Yu S Q, Ding D and Zhang Y-H 2003 GaAsSb/GaAs band alignment evaluation for long-wave photonic applications *J. Cryst. Growth* **251** 521–5
[92] Wei S-H and Zunger A 1995 InAsSb/InAs: A type-I or a type-II band alignment *Phys. Rev. B* **52** 12039–44
[93] Pryor C E and Pistol M-E 2005 Band-edge diagrams for strained III–V semiconductor quantum wells, wires, and dots *Phys. Rev. B* **72** 205311
[94] Ahtapodov L, Todorovic J, Olk P, Mjåland T, Slåttnes P, Dheeraj D L, van Helvoort A T J, Fimland B-O and Weman H 2012 A Story Told by a Single Nanowire: Optical Properties of Wurtzite GaAs *Nano Lett.* **12** 6090–5
[95] Vainorius N, Jacobsson D, Lehmann S, Gustafsson A, Dick K A, Samuelson L and Pistol M-E 2014 Observation of type-II recombination in single wurtzite/zinc-blende GaAs heterojunction nanowires *Phys. Rev. B* **89** 165423
[96] Möller M, de Lima Jr M M, Cantarero A, Chiaramonte T, Cotta M A and Iikawa F 2012 Optical emission of InAs nanowires *Nanotechnology* **23** 375704
[97] Ruda H E and Shik A 2005 Polarization-sensitive optical phenomena in semiconducting and metallic nanowires *Phys. Rev. B* **72** 115308
[98] Ketterer B, Heiss M, Uccelli E, Arbiol J and Fontcuberta i Morral A 2011 Untangling the Electronic Band Structure of Wurtzite GaAs Nanowires by Resonant Raman Spectroscopy *ACS Nano* **5** 7585–92
[99] Demichel O, Heiss M, Bleuse J, Mariette H and Fontcuberta i Morral A 2010 Impact of surfaces on the optical properties of GaAs nanowires *Appl. Phys. Lett.* **97** 201907
[100] Yuan X, Caroff P, Wang F, Guo Y, Wang Y, Jackson H E, Smith L M, Tan H H and Jagadish C 2015 Antimony Induced {112}A Faceted Triangular $GaAs_{1-x}Sb_x$/InP Core/Shell Nanowires and Their Enhanced Optical Quality *Adv. Funct. Mater.* **25** 5300–8
[101] Koblmüller G and Abstreiter G 2014 Growth and properties of InGaAs nanowires on silicon *Phys. status solidi - Rapid Res. Lett.* **8** 11–30
[102] Munshi A M, Dheeraj D L, Fauske V T, Kim D C, Huh J, Reinertsen J F, Ahtapodov L, Lee K D, Heidari B, van Helvoort A T J, Fimland B O and Weman H 2014 Position-Controlled Uniform GaAs Nanowires on Silicon using Nanoimprint Lithography *Nano Lett.* **14** 960–6
[103] Wallentin J, Anttu N, Asoli D, Huffman M, Aberg I, Magnusson M H, Siefer G, Fuss-Kailuweit P, Dimroth F, Witzigmann B, Xu H Q, Samuelson L, Deppert K and Borgstrom M T 2013 InP Nanowire Array Solar Cells Achieving 13.8% Efficiency by Exceeding the Ray Optics Limit *Science.* **339** 1057–60
[104] Stettner T, Kostenbader T, Ruhstorfer D, Bissinger J, Riedl H, Kaniber M, Koblmüller G and Finley J J 2017 Direct Coupling of Coherent Emission from Site-Selectively Grown III–V Nanowire Lasers into Proximal Silicon Waveguides *ACS Photonics* **4** 2537–43
[105] Svensson J, Anttu N, Vainorius N, Borg B M and Wernersson L-E 2013 Diameter-Dependent Photocurrent in InAsSb Nanowire Infrared Photodetectors *Nano Lett.* **13** 1380–5
[106] Thompson M D, Alhodaib A, Craig A P, Robson A, Aziz A, Krier A, Svensson J, Wernersson L-E, Sanchez A M and Marshall A R J 2016 Low Leakage-Current InAsSb Nanowire Photodetectors on Silicon *Nano Lett.* **16** 182–7
[107] Svensson J, Chen Y, Anttu N, Pistol M-E and Wernersson L-E 2017 Increased absorption in InAsSb nanowire clusters through coupled optical modes *Appl. Phys. Lett.* **110** 081104
[108] Robson M, Azizur-Rahman K M, Parent D, Wojdylo P, Thompson D A and LaPierre R R 2017 Multispectral absorptance from large-diameter InAsSb nanowire arrays in a single epitaxial growth on silicon *Nano Futur.* **1** 035001
[109] Ren D, Azizur-Rahman K M, Rong Z, Juang B-C, Somasundaram S, Shahili M, Farrell A C, Williams B S and Huffaker D L 2019 Room-Temperature Midwavelength Infrared InAsSb Nanowire Photodetector Arrays with Al 2 O 3 Passivation *Nano Lett.* acs.nanolett.8b04420
[110] Li Z, Trendafilov S, Allen M, Allen J, Alabadla A, Gao Q, Yuan X, Yang I, Caroff P, Tan H H, Jagadish C and Fu L 2018 Room Temperature GaAsSb Array Photodetectors *2018 IEEE Research and Applications of Photonics In Defense Conference (RAPID)* (IEEE) pp 1–3
[111] Li Z, Yuan X, Fu L, Peng K, Wang F, Fu X, Caroff P, White T

P, Hoe Tan H and Jagadish C 2015 Room temperature GaAsSb single nanowire infrared photodetectors *Nanotechnology* **26** 445202

[112] Yuan X, Saxena D, Caroff P, Wang F, Lockrey M, Mokkapati S, Tan H H and Jagadish C 2017 Strong Amplified Spontaneous Emission from High Quality $GaAs_{1-x}Sb_x$ Single Quantum Well Nanowires *J. Phys. Chem. C* **121** 8636–44

[113] Hjalmarson H P and Kurtz S R 1996 Electron Auger processes in mid-infrared InAsSb/InGaAs heterostructures *Appl. Phys. Lett.* **69** 949–51

[114] Alhodaib A, Noori Y J, Carrington P J, Sanchez A M, Thompson M D, Young R J, Krier A and Marshall A R J 2018 Room-Temperature Mid-Infrared Emission from Faceted InAsSb Multi Quantum Wells Embedded in InAs Nanowires *Nano Lett.* **18** 235–40

[115] Ren D, Farrell A C and Huffaker D L 2018 Axial InAs(Sb) inserts in selective-area InAsP nanowires on InP for optoelectronics beyond 25 μm *Opt. Mater. Express* **8** 1075

[116] Ahmad E, Kasanaboina P K, Karim M R, Sharma M, Reynolds C L, Liu Y and Iyer S 2016 Te incorporation in $GaAs_{1-x}Sb_x$ nanowires and p-i-n axial structure *Semicond. Sci. Technol.* **31** 125001

[117] Zhuang Q D, Alradhi H, Jin Z M, Chen X R, Shao J, Chen X, Sanchez A M, Cao Y C, Liu J Y, Yates P, Durose K and Jin C J 2017 Optically efficient InAsSb nanowires for silicon-based mid-wavelength infrared optoelectronics *Nanotechnology* **28** 105710